Thickness determination in anisotropic media with plasmon waveguide resonance imaging

Etienne Harté, Isabel Alves, Ivo Ihrke, Juan Elezgaray

Research Article | Vol. 27, No. 3 | 4 Feb 2019 | OPTICS EXPRESS 3264
Optics EXPRESS

Thickness determination in anisotropic media with plasmon waveguide resonance imaging

ETIENNE HARTÉ,[1] ISABEL D. ALVES,[2] IVO IHRKE,[3] AND JUAN ELEZGARAY[2,*]

[1] *LOMA, CNRS, University of Bordeaux, 33406 Talence, France*
[2] *CBMN, CNRS, INP Bordeaux, University of Bordeaux, 14 allée Saint Hilaire, 33600 Pessac, France*
[3] *LP2N, University of Bordeaux, INRIA, Av. François Mitterrand, 33400 Talence, France*
[*] *juan.elezgaray@u-bordeaux.fr*

Abstract: This paper describes a simple procedure to determine the local thickness of a thin anisotropic layer. It also discriminates between isotropic and anisotropic regions, provided a smoothness hypothesis on the refractive index distribution is satisfied. The procedure is based on the analysis of surface plasmon resonance (SPR) data acquired in an imaging mode. The general arrangement of the setup is the Kretschmann configuration. We show, on an azobenzene modified polymer layer, good agreement between atomic force microscopy and optical measurements of thickness variation.

1. Introduction

Anisotropic thin films are ubiquitous in many fields, from optical technologies to biophysical and cellular studies. Determination of both thickness and anisotropy characteristics of thin films is an important task in these fields. More generally, scanning a thin (100nm) slab of a sample can be mandatory in the characterization of highly structured media, such as adherent cells, where integrating across the whole sample can only provide with an average view of the cell. Common optical biosensing methods, such as surface plasmon resonance (SPR), optical waveguide spectroscopy (OWLS) and plasmon waveguide resonance (PWR) rely on the existence of discrete, localized modes which can be excited under particular conditions of the incident light. Each mode corresponds to an abrupt drop in the reflectivity. Tiny changes in the boundary conditions of the regions supporting localized modes dramatically change the excitation conditions. This high sensitivity is at the origin of the usefulness of SPR, OWLS and PWR. Anisotropy determination requires the use of two polarizations. Dual polarization interferometry (DPI) [1], the combined use of SPR and OWLS [2], or PWR [3,4] have been used in the past to characterize anisotropic thin samples. For the same reason, methods such as SPR where only one of the incident polarizations (p-polarization in the case of SPR) can excite localized modes, are not well suited to anisotropy measurements.

The determination of the spatial distribution of anisotropy characteristics over the sample is a further requirement in biophysical applications, where the existence of lateral heterogeneity (lipid domains [5] or rafts, protein domains as amyloid [3], cell adhesion regions) convey important functional information. In contrast with the good localization properties of SPR or PWR modes in the direction normal to the film, the lateral extension [6] of these modes is only limited by radiation losses. As an example, whereas the penetration depth of a typical SPR mode is $\sim$ 100 nm, its lateral decay length is more in the range of 10μm, which severely limits the expected spatial resolution [7]. The use of oil- immersion lenses to couple light into plasmon or guided modes is an alternative to the so-called Kretschmann configuration, where a prism plays the role of the coupler. It has been shown [8,9] that large numerical aperture objectives, combined with radial polarization substantially restrain the lateral propagation of plasmon modes. In turn, imaging in these configurations requires scanning: to form an image, the relative position between

Optics EXPRESS

the sample and the incident light needs to be changed. This severely limits the application of scanning methods to real time imaging.

The simultaneous determination of optical indices and thickness is a more challenging task. In the simplest isotropic case, it is usual to consider that at least two independent measurements of the same sample are required (this is also the case with ellipsometry). Notice however that, as it was shown in [10], accurate measurement of two different regions of the usual SPR response are enough to resolve the apparent ambiguity of thickness determination. It is presumable that this ideal situation cannot be translated to usual, non-ideal samples. In the context of biophysical studies, the so-called two-color and two-media approaches [11, 12] have been extensively used. In the two-color approach [12], two different wavelengths are required, which assumes that dispersion function of the sample is known. The two-media [11] approach requires performing two experiments with different external media, which can generate unwanted degradation of the sample. Alternatively, the use of two rotated versions of the same sample, as in [13], provides enough data to simultaneously measure thickness and optical index. More recently [14], use of either two metals or two thicknesses has been successfully considered in SPR experiments. Finally, [15] describes a setup very similar to ours, without any analysis of anisotropy determination.

This short review shows that the optical characterization of anisotropic films requires either complex setups or additional information (such as in the two-color method) which are not always available. A simple counting argument shows that there is no easy escape to this situation. In fact, in the most general case of an anisotropic medium, the number of unknowns to be determined is four (n_x, n_y, n_z, d): here, the optical indices are denoted by (n_x, n_y, n_z) and the unknown thickness by d. Therefore, to characterize a given homogeneous anisotropic film, at least four independent data are required. As an example, the routine use of PWR in biophysical studies focuses on the angular position of the two minima of reflectivity, corresponding respectively to the s (TE component that is perpendicular to the plane of incidence of the light) and p (TM component that is parallel to the plane of incidence of the light) resonances. The two remaining data can be obtained either by a change of the incident wavelength, or, in the case of a single available wavelength, by a rotation of the sample. In this paper, we show that anisotropic regions can be detected when only two measurements are present (as in standard PWR) provided some smoothness of the sample is assumed. The idea is that virtually any PWR spectrum can be modeled by stacking isotropic layers (an example is given below). However, when the underlying system is anisotropic, the isotropic model leads to variations of the values of the optical index which can easily be discarded based on physical arguments. Regions with such strong variations are putative candidates for anisotropic regions.

In this paper, we undertake the imaging of an inhomogeneous and anisotropic azobenzene polymer film using a simple adaptation of the usual PWR setup for the imaging mode. We then introduce an image analysis tool that discriminates between isotropic and anisotropic media. We compare both topography and optical indices to, respectively, AFM measurements and published results in the literature, obtaining respectively good and qualitative agreement. In the following, our imaging setup will be called Plasmon Waveguide Resonance Imager (PWRi).

2. Plasmon waveguide resonance imaging setup

The PWRi setup is the assembly of four units: (i) a light source shaped to the requirements (collimated beam, limited spectral width, and size), (ii) a sensor and Teflon cell for liquid samples positioned accurately, (iii) a custom built microscope allowing to image the inner surface of the sensor, and (iv) a scanning unit for adjusting the angle of incidence of the illuminating beam.

i The PWRi setup uses a LED light source emitting at 625 nm (Thorlabs, M625F2) filtered with a bandpass filter (center wavelength 630 nm, bandpass 3 nm) that feeds an optical fiber (Thorlabs, ML14) and is then collimated with a F280SMA-B package. The beam

Optics EXPRESS

is randomly polarized. The diameter of the optical fiber (50 μm) and the focal length (18.24mm) of the collimating lens determine the beam divergence in the collimated output beam (0.078°) and determine the limit of the angular system resolution.

ii The sensor is a SF11 isosceles prism (MT-Optics, China) whose angles are 50°, 50° and 80°. The prism is coated by 50 nm of silver and 460 nm of SiO_2 (Evaporated Coatings, USA). An adherence layer, the exact nature of which was not communicated by the provider, increases the adhesion between the prism and the metallic layer. The choice of the prism shape is dictated by the angle range where resonances are expected while having an essentially orthogonal incidence of the illuminating beam into the prism.

iii The imaging part is constituted of a Nikon 10x objective (NA=0.3), a Nikon tube lens (Thorlabs, ITL200) and a camera (Point Grey Grasshoper 3). The imaging system is arranged such that its optical axis is orthogonal to the prism face on the observation side. This measure minimizes the aberrations introduced by the planar air/glass interface of the prism. On the down-side, the coated object plane of the prism is now at a significant angle to the optical axis of the system and imaging occurs in the Scheimpflug condition [16], i.e. the image plane is tilted with respect to the optical axis as well. In our setup, the object plane is at 50° to the optical axis, which results in a Scheimpflug image plane tilt of about 75.5°. Ideally, in order to image the complete field sharply, the sensor would be positioned at this tilt angle with respect to the optical axis. On the other hand, the camera pixel sensitivity decreases with the incidence angle of light. In particular, the microlenses used in modern sensors to increase the light gathering area also reduce the pixel sensitivity at steep angles, in addition to the expected cosine-falloff. In practice, we choose a sensor tilt of 43.2° as a trade-off between the extent of the sharp field and an acceptable signal-to-noise ratio. The imaging geometry also induces a non-uniform distortion principally along the two orthogonal image axes. This distortion depends on the incidence angle of the illumination beam since the reflected wave passes the imaging system differently for different angles. We digitally compensate for these distortions by performing a calibration measurement with a known grid (PDMS) for the range of illumination angles of interest.

iv The rotation stage (NEWPORT, RGV100BL) that controls the angle of incidence of the light source has a resolution below 0.001° which is well below the angular beam divergence of the illumination beam. A PWRi measurement consists in measuring the light intensity as a function of incidence angle of the light. This angle is monitored by the rotation of the light source around the fixed parts (microscope and sensor) as shown in Fig. 1. A typical spectrum is shown in Fig. 2: the two minima correspond, respectively, to the *p* and *s* polarized components of the incident light. The experimental spectrum shows several distortions from the theoretical spectrum shown in Fig. 2: both an intensity drift for higher values of incidence and randomly distributed fluctuations. The drift could be due to a non homogeneity of the incident beam, whereas the random fluctuations could be related to irregularities (dust) on the prism arising from the spin coat step in the preparation of the sample.

3. Azobenzene based polymer layer as a reference sample

We validate the imaging capabilities of PWRi with a material whose anisotropy can be spatially controlled. UV irradiation of organic thin films may induce changes in the refractive index (cf. [17] for a recent work). Polymers containing azo dyes were first studied by Todorov and coworkers [18], who showed, since the 1980s, that anisotropy could be monitored by irradiation with polarized light. More precisely, polymers containing azo-dyes present the capacity to orient themselves perpendicularly to the electric field upon light irradiation [19, 20]. Accordingly,

Optics EXPRESS

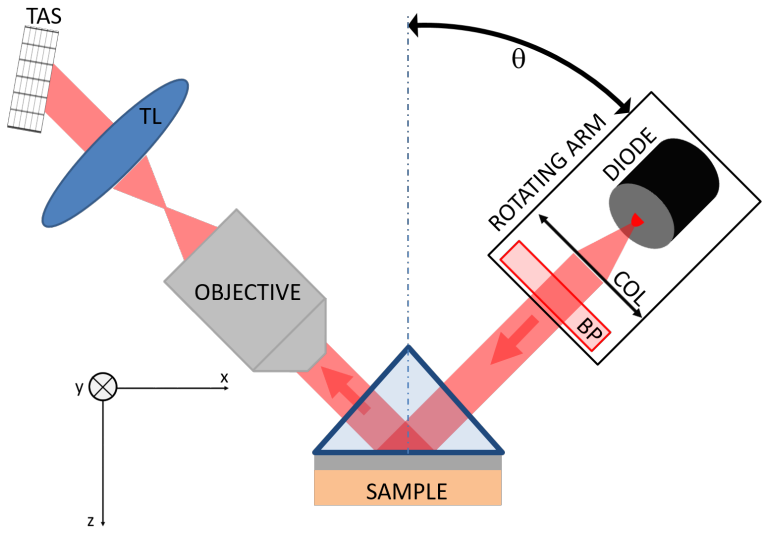

Fig. 1. Schematic representation of the PWRi setup. COL is a collimator converting the divergent light of the 525 nm diode into a parallel beam filtered with BP, a 3 nm-bandpass filter centered at 630 nm. The objective collects the light and an image is formed on the tilted camera TAS via TL, the tube lens of the infinity-corrected microscope objective. θ is the angle of incidence of the beam on the sample, as well as the angle under which the sample is being observed.The prism is fixed on an optical post. The rotation stage is a ring with an empty central area. This allows the optical post supporting the prism to be installed inside the free space located at center of the ring.

depending on the polarization of the incident light, the local anisotropy can be monitored, leading to 2D or 3D anisotropic materials. For the preparation of the thin layer, we used the polymer DR1 co MMA (Specific Polymers, SP-NLO-P-008). It was diluted in chloroform at a concentration of 5 mg/mL. To deposit a thin polymer film, 35 μL of the above solution were spin coated on the PWR sensor at 1600 rpm for 60s. The sample was then annealed by heating at 120 °C for 1 h. After annealing, the film was assumed isotropic. By using a focused laser beam and a motorized microscope stage, an irradiation pattern was applied to the spin-coated polymer sample [21] to induce controlled changes in the anisotropy of the sample to be analyzed with the PWRi setup. As engraving source, we used a WITec Alpha 300 Raman confocal Microscope (532 nm laser as actinide light source, objective NIKON 5x, NA=0.1). Modification of the anisotropy was done by moving the sample continuously at a speed of 1.5 μm/s. A $\lambda/2$ plate was used to rotate the polarization of the actinide beam. The induced anisotropy has been shown to be stable for at least a few days [22, 23]. In our case, the pattern consisted of four lines, 150 μm long (Fig. 3), aligned along the x-axis. Two of them (1 and 2) were engraved at 50 μW and the other two (3 and 4) with a higher 2mW power. The linear polarization of the incident beam was along the x-axis for 1 and 3, along the y-axis for 2 and 4. Note that the width ($\sim$ 5 μm) of the lines is related to the width of the beam.

Irradiation with polarized light not only induces anisotropy: when the wavelength matches the absorption of the azobenzene moiety, mass transport with associated topographic changes can be observed [24]. The azo moities induce migration in a direction along the polarization vector, from large towards small intensity regions. This phenomenon has been extensively used in the production of holograms and depends, among other factors, on the extent of irradiation. This property has also been used [25] to map electric field distributions around metallic structures. In

Optics EXPRESS

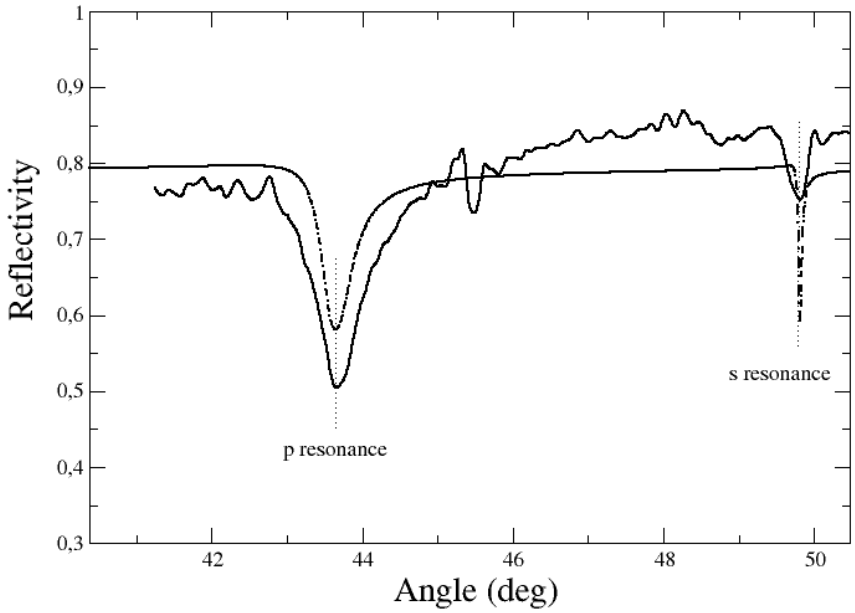

Fig. 2. Comparison between the measured (continuous line) and computed (dashed line) reflectance spectra obtained with *p*- (minimum located near 43.5°) and *s*-polarized light (minimum located near 49.5°). Vertical dotted lines correspond to the angular position of the two minima.

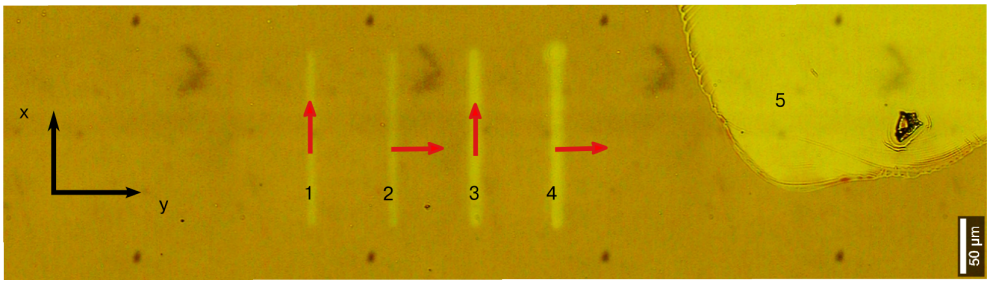

Fig. 3. Optical image of the azo-coating, patterned along the four lines 1, 2, 3 and 4. The region 5 corresponds to an uncoated region. It was used as a reference for the PWRi spectra. Red arrows indicate the polarization used to engrave each line. Molecules are preferentially oriented perpendicular to the polarization. As an example, molecules in line 2 will be preferentially oriented along the x axes.

our case, the result was a depletion of the irradiated zones, with a corresponding mass migration to the borders of each irradiation line. Topography profiles, as obtained from atomic force microscopy (AFM) imaging (peak force mode, as implement in a FastScan Bruker AFM), are represented in Fig. 4. Patterns 1 and 2 are shallower than patterns 3 and 4, in agreement with the respective time of irradiation.

Optics EXPRESS

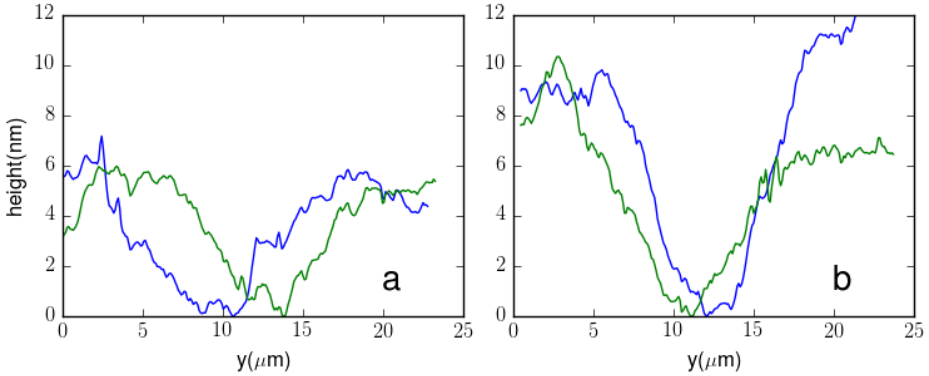

Fig. 4. a) Topography profiles across the low-power (lanes 1 and 2 from Fig. 3) and b) high-power (lanes 3 and 4 from Fig. 3) patterns, with polarization of the engraving laser being parallel (blue), or perpendicular (green) to the engraving direction. The depth variation of the pattern is ~ 6 nm (low intensity) and ~10 nm for the high-power pattern.

4. Thickness estimation and comparison with AFM measurements.

Anisotropy measurements and thickness estimation have already been reported by several groups. 2D measurement of the refractive indices of a ~ 2 μm thick polymer layer was performed [26], taking advantage of the prism coupled modes of resonance of a waveguide (cf. [17] for a related work). 3D determination of the refractive index was also reported for Azo containing polymers with modulated polarimetry [27], a set of three probe lasers [28], a combination of ellipsometry techniques [29] and waveguide spectroscopy [13]. However, none of these publications reported on the lateral resolution, an additional aspect that is treated here by the imaging mode. Figure 5 reports a striking demonstration of the discriminating power of the PWRi imager. PWRi spectra, measured at four different incident angles selected around the *s*-resonance, show clear differences between patterns 3 and 4 (respectively 1 and 2), even though these two patterns have been engraved with the same intensity and, consequently, have very similar topographic properties. For instance, pattern 3 is hardly seen in Fig. 5(a). In the same way, pattern 1 is not clearly shown in Fig. 5(c). However, as mentioned in the introduction, one should be cautious about the interpretation of these PWRi spectra because from a single PWRi spectrum, it is a priori difficult to distinguish between thickness variations and anisotropy variations. To go beyond, we fitted the PWRi data to a simple model of stacked isotropic layers. To simplify the discussion, in the following we will ignore the x direction (along the engraved patterns) and will only consider variations along the y direction.

For each angle of incidence, the CCD camera records an image. Therefore, for each pixel, a curve $I(x, y, \theta)$ is obtained. Averaging along the x direction leads to a simplified set $I_{ave}(y, \theta)$ of data. These data were fitted to a multilayer model, as implemented in the free software py_matrix [30], based on a particular implementation of the matrix formalism [31] for multilayer structures. The fitting was based on the standard Python implementation of the Nelder-Mead (or downhill) simplex method [32]. The model contains four layers, 3 for the sensor and 1 for the sample. The sensor layers model the adhesive layer and silver layers and a third layer made of silica. The sample layer is modeled as a polymer layer with unknown thickness (d) and three optical indices (n_x, n_y, n_z). Under the isotropy assumption ($n_x = n_y = n_z = n$), the two parameters (n, d) were adjusted so as to fit the position of the two minima of each $I_{ave}(y, \theta)$ data set (Fig. 2). For each case, parameters were optimized until the error in the angular position of

Optics EXPRESS

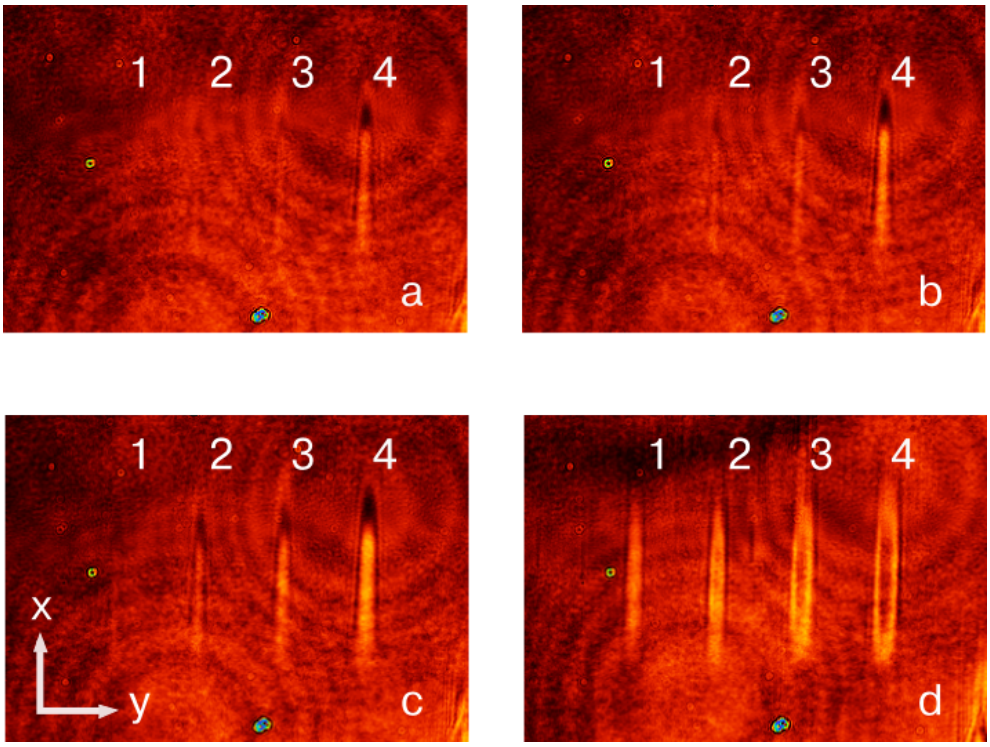

Fig. 5. PWRi images as measured at four different incident angles, successively (a) 49.33°, (b) 49.449°, (c) 49.504° and (d) 49.654°. 1, 2, 3 and 4 label each of the engraved patterns.

the minima was less than the rotational precision of the motor (0.001°). The accuracy in the thickness determination of the SPR sensor layers (metal and dielectric) deserves some discussion. Because of the plasma cleaning step needed to ensure the adhesion of the polymer layer, the actual thickness of the waveguide is not the thickness of the sensor as provided by the fabricant, which was 450±50nm. To estimate this thickness, we fitted the spectra obtained by imaging the region 5 in Fig. 3. However, as illustrated in Fig. 2, this fit only attempts to match the angular position of the PWRi spectrum, other features such as the width and depth of the resonant peaks can only qualitatively modelized by a stack of planar layers. Possible origins of the difference from an ideal PWR detector include the roughness induced by the plasma cleaning procedure and optical aberrations enhanced by the divergence of the incident beam, none of which were taken into account in the fitting procedure. An additional source of uncertainty is the unknown nature of the adhesion layer, which was not communicated by the manufacturer. In the absence of this information, we assumed its refractive index to be close to that of chromium, a popular glue used for this purpose. Taking into account all these approximations, we considered two different methods to estimate the uncertainty on the thickness measurement. The first method is based on the uncertainty (±0.006°) on the position of resonances arising from the discreteness of rotation steps. If an averaged PWR spectrum (along the x direction) is considered, an uncertainty < 1 nm is obtained. Clearly, this is not very realistic. The second method estimates the uncertainty by fitting non averaged PWRi spectra obtained at different points of region 5. The value obtained (~ 40 nm) is more in line with the uncertainty value provided by the manufacturer (~ 50 nm). In view of all the approximations of the model, it should only be considered as a lower bound. Finally, it should be stressed that the fitting is based on an approximation by a stack of plane layers. This implicitly assumes that geometrical optics is valid, as discussed in [6], and that only

Optics EXPRESS

a spatially smoothed version of the topography and index distribution can be measured.

Figure 6 shows the result of the isotropic approximation. The thickness profile shows two dips at the expected position of patterns 1 and 3, with depths of 4 and 8 nm, respectively. No such variations are apparent at expected positions of patterns 2 and 4. In contrast, the refractive index n shows strong variations (15%) at these points. Comparison with reported optical index values after azo- reorientation [10], where the variations upon irradiation are more in the range of 1-2%, suggests that these values could be considered as artifacts of the isotropic hypothesis. As an alternative to the isotropic model, averaged $I_{ave}(y, \theta)$ data can be fitted by an anisotropic model. Because we only consider two angular positions as constraints to the model, several combinations of (n_x, n_y, n_z, d) fit a given PWRi spectrum. More precisely, for each value of y, a one-parameter family $(n_x(d), n_y(d), n_z(d), d)$ of possible solutions can be found, parametrized by the unknown thickness d. The procedure to find such a family of solutions is straightforward: for each y-value, choose a candidate thickness value d, fit the angular position of the s- resonance, which only depends upon $n_y(d)$, then find the couple $(n_x(d), n_z(d))$ that matches the angular position of the p-resonance.

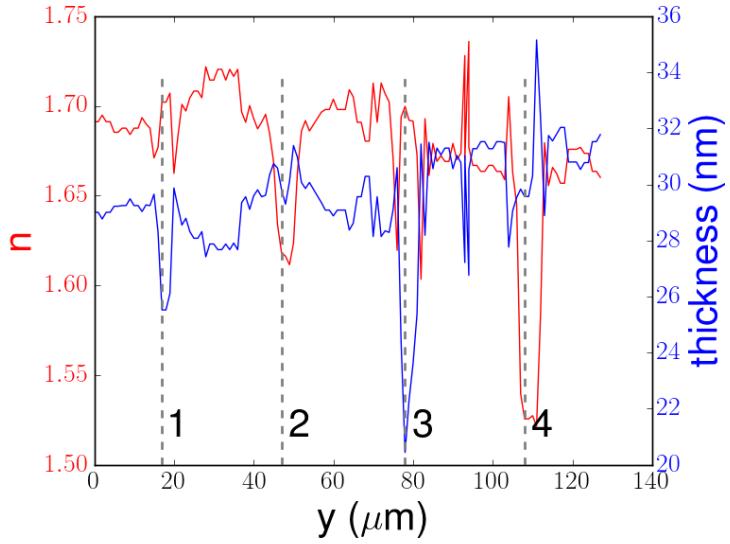

Fig. 6. Thickness (blue) and refractive index (red) determination under the isotropic hypothesis. Gray dashed lines point to places where engraved patterns are expected. Positions of the patterns 1 and 3 are correctly captured by the isotropic model, on the opposite, patterns 2 and 4 are completely missed.

The remaining problem is to find a particular thickness profile $d(y)$. Let us note $\vec{n}(y) = \vec{n}(d(y))$ the 3D optical index that fits as much as possible the position of the s and p resonances for a given thickness $d(y)$ at coordinate y. As a matter of fact, many profiles $d(y)$ give a reasonable fit of the two resonances, in other words, this problem is ill-posed. This can be understood easily as four parameters (n_x, n_y, n_z) and $d(y))$ are available to fit two data. Therefore, to select a unique profile, additional constraints need to be introduced. Here, we hypothesize that the actual index distribution corresponds to solutions where spatial variations of optical index are 'small', in other words, we pick the particular profile $d(y)$ which minimizes the following cost function:

$$C = \int ||\frac{d\vec{n}}{dy}||^2 + a(n_x - n_y)^2 + a(n_x - n_z)^2 + F(\vec{n})dy \quad (1)$$

In this expression, the first term of the cost function C tends to favor smooth variations of

$\vec{n}(y)$, whereas the second term tends to favor isotropic profiles. The parameter a is used to select the trade-off between the two conditions. When a increases, isotropic solutions are picked, possibly showing sharp variations, as in Fig. 6. On the opposite, when $a = 0$, we observed that anisotropic solutions in homogeneous regions of the sample can be selected. The last term of the cost function constrains the function $\vec{n}(y)$ to be the one that fits as much as possible the experimental data: $F(\vec{n}(y)) = (\theta_1^{exp} - \theta_1)^2 + (\theta_2^{exp} - \theta_2)^2$, where $\theta_{1,2}$ (respectively $\theta_{1,2}^{exp}$) are the angular positions of the resonances (respectively experimental data).

Numerically, the minimization of the cost function was done starting at positions where it is known that the system is isotropic, then propagating this solution for increasing (or decreasing values) of y. For each of these values, the cost function was computed for a discrete set of values $d(y)$, which explains the discrete character of the dotted lines in Fig. 7. This figure represents three thickness profiles obtained after minimization of the cost function C for $a = \infty, a = 10$ and $a = 0.1$, respectively. As expected, the $a = 10$ solution resembles the isotropic case $a = \infty$. In turn, the $a = 0.1$ solution correctly selects the dips at positions 2 and 4, while preserving those at positions 1 and 3. When compared to AFM images (Fig. 4), depth profiles obtained with the anisotropic model correspond to smoothed (shallower) versions of the topography. This should be expected, as optical images necessarily encompass some spatial averaging.

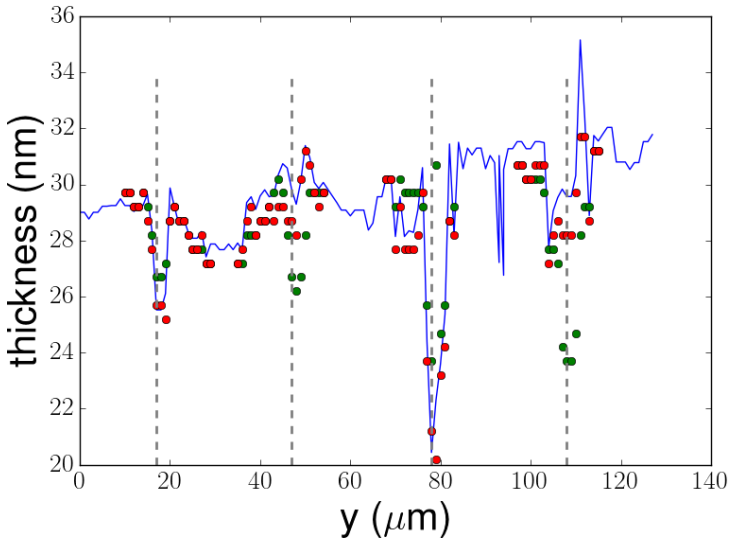

Fig. 7. Determination of the polymer thickness with, respectively, the isotropic model (blue line), anisotropic model a = 0.1 (green dots) and a = 10 (red dots). Grey dashed lines point to places where engraved patterns are expected.

The values of the anisotropic indices obtained for $a = 0.1$ are reported in Fig. 8, and are compared to the isotropic index. As expected, the relative variations are milder than in the isotropic model. We also note that $n_x < n_y$ for patterns 1 and 3, but $n_y < n_x$ for patterns 2 and 4, as expected since azobenzene molecules reorient mainly perpendicular to the linear polarization of the incident light [25]. One can also note that the birefringence increases with the time of irradiation. Similar values have been reported previously in the literature [26].

5. Conclusions

We have introduced an imaging method, PWRi, based on the coupling between plasmon and waveguided modes. The experimental setup is a straightforward generalization of the usual,

Optics EXPRESS

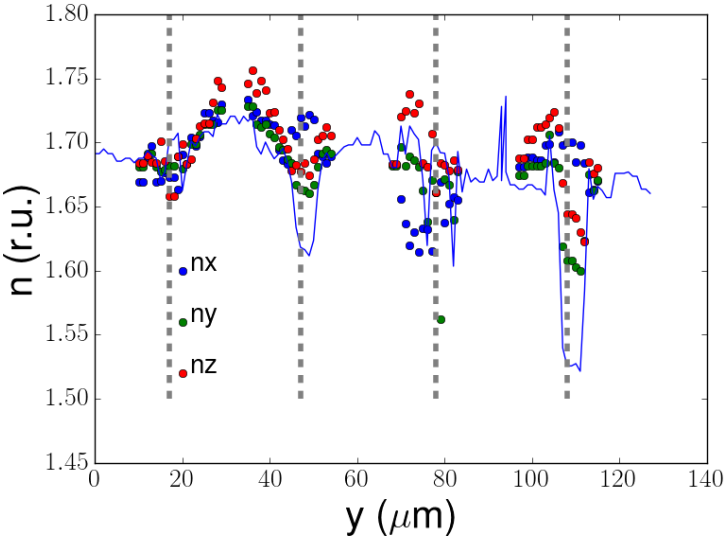

Fig. 8. Anisotropic optical indices, as determined from the minimization of the cost function C for $a = 0.1$. Colors are: blue (n_x), green (n_y) and red (n_z). The continuous line corresponds to the isotropic model. Grey dashed lines point to places where engraved patterns are expected.

prism based, configuration. We have shown, on a particular anisotropic sample, that the mere tracking of the angular position of the s and p resonances, provides useful information on the position of anisotropic regions. Minimizing the cost function improves the blunt predictions of the isotropic model, selecting among the infinite set of solutions compatible with the angular position of the s and p resonances. This considerably simplifies previous existing methods to capture anisotropy. Topography recovered from PWRi corresponds to a spatially averaged image of the 'real' topography, as measured by AFM. The present work should be considered as a first step towards a more accurate method of anisotropy imaging. In particular, an accurate determination of *absolute values* of thickness and refractive index was not possible in the present version of the PWRi setup, even for the isotropic samples. The question remains how to choose the parameter a that controls the relative weight between spatial gradients and anisotropy. Future work will consider the use of automatic ways [33] to determine its optimal value. Additional work will also be needed to validate the method in more complex, two dimensional anisotropy profiles.

Funding

Défi Imag'In, CNRS.

References

1. A. Mashaghi, M. Swann, J. Popplewell, M. Textor, and E. Reimhult, "Optical anisotropy of supported lipid structures probed by waveguide spectroscopy and its application to study of supported lipid bilayer formation kinetics," Anal. Chem. **80**, 3666–3676 (2008).
2. K. Tawa and W. Knoll, "Out-of-plane photoreorientation of azo dyes in polymer thin films studied by surface plasmon resonance spectroscopy," Macromolecules **35**, 7018–7023 (2002).
3. E. Harté, N. Maalouli, A. Shalabney, E. Texier, K. Berthelot, S. Lecomte, and I. Alves, "Probing the kinetics of lipid membrane formation and the interaction of a nontoxic and a toxic amyloid with plasmon waveguide resonance," Chem. Commun. **50**, 4168–4171 (2014).

Optics EXPRESS

4. Z. Salamon, H. A. Macleod, and G. Tollin, "Coupled plasmon-waveguide resonators: A new spectroscopic tool for probing proteolipid film structure and properties," Biophys J. **73**, 2791–2797 (1997).
5. Z. Salamon, S. Devanathan, I. D. Alves, and G. Tollin., "Plasmon-waveguide resonance studies of lateral segregation of lipids and proteins into microdomains (Rafts) in solid-supported bilayers," J. Biol. Chem. **280**, 11175–11184 (2005).
6. L. Laplatine, L. Leroy, R. Calemczuk, D. Baganizi, P. N. Marche, Y. Roupioz, and T. Livache, "Spatial resolution in prism- based surface plasmon resonance microscopy," Opt Express **22**, 22771–22785 (2014).
7. W. Hickel and W. Knoll, "Surface plasmon optical characterization of lipid monolayers at 5um lateral resolution," J. Appl. Phys. **67**, 3572–3575 (1990).
8. M. G. Somekh, S. G. Liu, T. S. Velinov, and C. W. See, "Optical V(z) for high-resolution 2π surface plasmon microscopy," Opt. Lett. **25**(11), 823–825 (2000).
9. L. Berguiga, S. J. Zhang, F. Argoul, and J. Elezgaray, "High resolution surface-plasmon imaging in air and water: V(z) curve and operating conditions," Opt. Lett. **32**(5), 509–511 (2007).
10. S. Cowen and J. R. Sambles, "Resolving the apparent ambiguity in determining the relative permittivity and thickness of a metal film using optical excitation of surface plasmon-polaritons," Opt. Comm. **79**(6), 427–430 (1990).
11. H. E. de Brujin, B. S. F. Altenburg, R. P. H. Kooyman, and J. Greve, "Determination of thickness and dielectric constant of thin transparent dielectric layers using Surface Plasmon Resonance," Opt. Comm. **82**(5-6), 425–432 (1991).
12. K. A. Peterlinz and R. Georgiadis, "Two-color approach for determination of thickness and dielectric constant of thin films using Surface Plasmon Resonance Spectroscopy," Opt. Comm. **130**(4-6), 260–266 (1996).
13. C. C. Jung, M. Rutloh, and J. Stumpe, "Waveguide spectroscopic characterization of 3D anisotropies in conventionally photooriented and annealed films of liquid crystalline and amorphous azobenzene polymers," J. Phys. Chem. B **109**(16), 7865–7871 (2005).
14. T. Del Rosso, J. E. Hernandez Sanchez, R. Dos Santos Carvalho, O. Pandoli, and M. Cremona, "Accurate and simultaneous measurement of thickness and refractive index of thermally evaporated thin organic films by surface plasmon resonance spectroscopy," Opt. Express **22**(16), 18914–18923 (2014).
15. N. Skievesen, R. Horvath, S. Thinggaard, N. B. Larsen, and H. C. Pedersen, "Deep-probe metal-clad waveguide biosensor," Biosens. Biolec. **22** 1282–1288 (2007).
16. M. Born and E. Wolf, *Principles of Optics* (Pergamon, 1987).
17. T. Del Rosso, Q. Zaman, M. Cremona, O. Pandoli, and A.R.J. Barreto, "SPR sensors for monitoring the degradation processes of Eu(dbm)3(phen) and Alq3 thin films under atmospheric and UVA exposure, " Appl. Surf. Sci. **442**, 759–766 (2018).
18. T. Todorov, N. Tomova, and L. Nikolova, "High-sensitivity material with reversible photo-induced anisotropy," Opt. Comm. **47**(2), 123–126 (1983).
19. J. Stumpe, L. Lasker, T. Fischer, M. Rutloh, S. Kostromin, and R. Ruhmann, "Photo-orientation in amorphous and aligned films of photochromic liquid crystalline polymers," Thin Solid Films **284-285**, 252–256 (1996).
20. C. C. Jung, R. Rosenhauer, M. Rutloh, C. Kempe, and J. Stumpe, "The generation of three-dimensional anisotropies in thin polymer films by angular selective photoproduct formation and annealing," Macromolecules **38**(10), 4324–4330 (2005).
21. S. Bian, L. Li, J. Kumar, D. Y. Kim, J. Williams, and S. K. Tripathy, "Single laser beam-induced surface deformation on azobenzene polymer films," Appl. Phys. Lett. **73**(13), 1817–1819 (1998).
22. Z. Sekkat and M. Dumont, "Photoinduced orientation of azo dyes in polymeric films. Characterization of molecular angular mobility," Synth. Met. **54**(1-3), 373–381 (1993).
23. A. Natansohn, P. Rochon, J. Gosselin, and S. Xie, "Azo polymers for reversible optical storage. 1. Poly[4'-[[2-(acryloyloxi)ethyl]ethylamino] -4 - nitroazobenzene]," Macromolecules **25**(8), 2268–2273 (1992).
24. A. Natansohn and P. Rochon, "Photoinduced motions in azo-containing polymers, " Chem. Rev. **102** 4139 (2002).
25. B. C. Galarreta, I. Rupar, A. Young, and F. Lagugné-Labarthet, "Mapping Hot-spots in hexagonal arrays of metallic nanotriangles with azobenzene polymer thin films," J. Phys. Chem. C **115** 15318–15323 (2011).
26. S. Morino, S. Machida, T. Yamashita, and K. Horie, "Photoinduced refractive index change and birefringence in poly(methyl methacrylate) containing p-(dimethylamino)azobenzene," J. Phys. Chem. **99**(25), 10280–10284 (1995).
27. C. I. Chuang, S. H. Lin, and Y. F. Chao, "Dynamic characterization of photo-alignment of azo-dye-doped polymer using phase modulated polarimetry," Opt. Mater. **35**(3), 366–371 (2013).
28. M. Dumont, "3D characterization of photo-induced anisotropy and all-optical poling of organic films," Nonlinear Opt. Quantum Opt. **43**(1-4), 239–257 (2012).
29. C. C. Jung and J. Stumpe, "Immersion transmission ellipsometry (ITE) for the determination of orientation gradients in photoalignment layers," Appl. Phys. B: Lasers Opt. **116** 533–539 (2014).
30. G. Pellegrini and G. Mattei, "High-Performance Magneto-Optic Surface Plasmon Resonance Sensor Design: An Optimization Approach," Plasmonics **9**(6), 1–6 (2014).
31. M. Mansuripur, "Analysis of multilayer thin-film structures containing magneto-optic and anisotropic media at oblique incidence using 2x2 matrices," J. Appl. Phys. **67** 6466 (1990).

Optics EXPRESS

32. B. P. Flannery, S. Teukolsky, W.H. Press, and W.T. Vetterling, Numerical Recipes in Fortran (Cambridge University, 1986).
33. P. C. Hansen and D. Prost O'Leary, "The use of the L-curve in the regularization of discrete ill-posed problems," SIAM J. on Sci. Comp. **14** 1487–1503 (1993).